HF Propagation Results From The Metal Oxide Space Cloud (MOSC) Experiment

Joshi, Dev; Groves, Keith; McNeil, William; Carrano, Charles ; Caton, Ronald; Parris, R Todd; Pedersen, Todd; Cannon, P.S.; Angling, Mathew; Jackson-Booth, Natasha

DOI:
10.1002/2016RS006164

AGU PUBLICATIONS

Radio Science

RESEARCH ARTICLE
10.1002/2016RS006164

Special Section:
2013 Equatorial Ionospheric Sounding Rocket Campaign from Kwajalein Atoll

HF propagation results from the Metal Oxide Space Cloud (MOSC) experiment

Dev Joshi[1,2], Keith M. Groves[1], William McNeil[1], Charles Carrano[1], Ronald G. Caton[3], Richard T. Parris[3], Todd R. Pederson[3], Paul S. Cannon[4,5], Matthew Angling[5], and Natasha Jackson-Booth[4]

[1]Institute for Scientific Research, Boston College, Chestnut Hill, Massachusetts, USA, [2]Department of Physics, Boston College, Chestnut Hill, Massachusetts, USA, [3]Space Vehicles Directorate, Air Force Research Laboratory, Kirtland Air Force Base, Albuquerque, New Mexico, USA, [4]QinetiQ, Malvern, United Kingdom, [5]Now at University of Birmingham, Birmingham, United Kingdom

Key Points:
- High-frequency propagation effects due to an artificial plasma cloud successfully modeled
- Effects of arbitrary plasma environments shown to be predicted with accuracy by ray-tracing
- Ray tracing can be applied to selectively adjust ionospheric models effectively for HF applications

Correspondence to:
D. Joshi,
dev.joshi@bc.edu

Citation:
Joshi, D., K. M. Groves, W. McNeil, C. Carrano, R. G. Caton, R. T. Parris, T. R. Pederson, P. S. Cannon, M. Angling, and N. Jackson-Booth (2017), HF propagation results from the Metal Oxide Space Cloud (MOSC) experiment, *Radio Sci.*, *52*, 710–722, doi:10.1002/2016RS006164.

Received 1 SEP 2016
Accepted 11 APR 2017
Accepted article online 25 APR 2017
Published online 1 JUN 2017

Abstract With support from the NASA sounding rocket program, the Air Force Research Laboratory launched two sounding rockets in the Kwajalein Atoll, Marshall Islands in May 2013 known as the Metal Oxide Space Cloud experiment. The rockets released samarium metal vapor at preselected altitudes in the lower *F* region that ionized forming a plasma cloud. Data from Advanced Research Project Agency Long-range Tracking and Identification Radar incoherent scatter radar and high-frequency (HF) radio links have been analyzed to understand the impacts of the artificial ionization on radio wave propagation. The HF radio wave ray-tracing toolbox PHaRLAP along with ionospheric models constrained by electron density profiles measured with the ALTAIR radar have been used to successfully model the effects of the cloud on HF propagation. Up to three new propagation paths were created by the artificial plasma injections. Observations and modeling confirm that the small amounts of ionized material injected in the lower *F* region resulted in significant changes to the natural HF propagation environment.

1. Introduction

Since the 1950s after the availability of rockets for research purposes, experiments have been conducted to inject various materials into the atmosphere for the purpose of creating perturbations to the ambient medium [*Bedinger et al.*, 1958; *Rosenberg*, 1963; *Corliss*, 1971; *Davis*, 1979; *Wand and Mendillo*, 1984; *Bernhardt et al.*, 2012]. Such ionospheric modification experiments in the form of chemical releases have been used for various goals such as to measure neutral wind directions and shears, to detect plasma drift velocities and electric fields, to exploit the ionosphere as a plasma laboratory without walls, to modify the plasma density in the ionosphere to trigger larger scale phenomena, and many other uses [*Bernhardt*, 1987; *Hu et al.*, 2011; *Shuman et al.*, 2015]. The Air Force Research Laboratory (AFRL) launched two sounding rockets in the Kwajalein Atoll, Marshall Islands, in May 2013 known as the Metal Oxide Space Cloud (MOSC) experiment. The sounding rockets, each carrying a payload of two 2.5 kg canisters of powdered samarium metal in a thermite mixture, released samarium metal vapor at dusk at 170 and 180 km altitude, respectively. A fraction of the samarium metal vapor ionized in the ambient environment, creating an additional layer of plasma. The objectives of the experiments were to understand the dynamics, evolution, and chemistry of Sm atoms in the Earth's upper atmosphere; to understand the interactions of artificial ionization and the background plasma; and to measure the effects on high-frequency (HF) radio wave propagation. A host of diagnostic instruments were used to probe and characterize the cloud including the Advanced Research Project Agency Long-range Tracking and Identification Radar (ALTAIR) incoherent scatter radar, multiple GPS, and optical instruments, satellite radio beacons, and a dedicated network of high-frequency (HF) radio links [*Caton et al.*, 2017]. In this paper, we report the results from the HF sounder observations and modeling those results with the ALTAIR radar data using the HF radio wave ray-tracing MATLAB toolbox PHaRLAP. The modeling results enable us to understand the changes caused by the samarium plasma cloud in the HF propagation environment and thus validate the extent to which we can model HF propagation for other specified plasma perturbations. We have developed a new technique to model an anomalous background ionosphere by assimilating oblique ionosonde data specifically to match observed HF signal delays. The approach may have numerous applications for ionospheric specification for HF propagation.

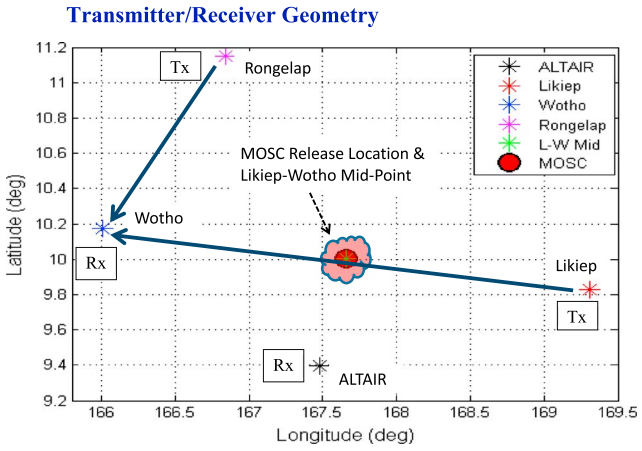

Figure 1. Site locations in Marshall Islands. Tx = transmitter, Rx = receiver. The MOSC release point is midway between Likiep and Wotho.

In Figure 1, the site locations corresponding to the HF links and the ALTAIR incoherent scatter radar are shown. In this work, we focus on the signals received at Wotho from transmitters at Rongelap and Likiep. The Rongelap-Wotho link geometry is predominantly N-S and the release region is far from the great circle path, whereas the Likiep-Wotho path is nearly magnetic E-W and the release point lies close to the midpoint of the link. Geographic coordinates for the sites may be found in Table 1.

The first sounding rocket launch occurred on 1 May 2013 at 07:38 UT, and the samarium metal vapor release occurred at 07:40:40 UT. The second sounding rocket launch occurred on 9 May 2013 at 07:23 UT, and the release occurred at 07:25:40 UT. In both releases, approximately 10% of the samarium metal in the canisters ionized.

2. Observations

The Advanced Research Project Agency Long-range Tracking and Identification Radar (ALTAIR) at Kwajalein Atoll was used to monitor the ionospheric state and track the evolution of the metal oxide space cloud. Range-time-intensity displays of each release event are shown in Figure 2. The data gap during the first release shown in Figure 2a was an intentional data management action to avoid a data file size limitation. Recording was turned off for a period of about 2 min and turned back on approximately 30 s prior to the samarium release. Improved prelaunch file management on the night of 9 May precluded the need to limit data sampling during the second rocket flight as shown in Figure 2b.

The ionograms (Figures 3 and 4) from the oblique sounder data for the releases on 1 and 9 May 2013 show the evolution of the ionosphere before and after the release of the samarium metal vapor in the ambient environment. Both Likiep and Rongelap used broadband folded dipole transmit antennas approximately 12 m long connected to 100 W power amplifiers to transmit swept frequency waveforms from 2–30 MHz every 5 min at the rate of 100 KHz/s. The timing for both transmitters and receivers was synchronized by GPS-disciplined clocks. The ionograms shown in the figures were recorded at Wotho using a simple 1 m diameter loop antenna. Plots show data from only 2–14 MHz since no signatures were observed at higher frequencies. The titles include the start time of the frequency sweep (2 MHz); end time at 14 MHz is 120 s later. In prerelease sweeps on 1 May, *E*-layer traces are also seen in the ionograms in addition to the ground wave and *F* region traces, whereas the *E*-layer trace is not seen on 9 May, suggesting that the *E* region is not present during the second release. The *E*-layer echoes present on 1 May are due to sporadic *E* [*Davies*, 1990], as the traces extend to 10 MHz or so, well beyond the peak plasma frequency expected in the *E* region at this local time (approximately 18:20 LT). The *F* region traces are further seen to be split into two characteristic components: ordinary and extraordinary waves. The effects of the artificial plasma cloud are clearly seen in the postrelease sweeps along both Rongelap-Wotho and Likiep-Wotho paths. Two additional traces, denoted as the "MOSC" layer and the secondary *F* region echo, are evident, suggesting significant change in the propagation environment of the HF radio waves due to the metal oxide plasma cloud. SmO+ layer density (approximately 10 MHz at early times) is similar in both cases and observed initially on all links. The density of the artificial cloud is observed to fall rapidly over time scales of a few minutes, and the signatures disappear completely within about 15 min. The difference between the secondary *F* region echo

Table 1. Geographic Co-Ordinates

Site	Latitude (°N)	Longitude (°E)
Rongelap	11.152	166.838
Likiep	9.826	169.307
Wotho	10.174	166.005
ALTAIR	9.395	167.479

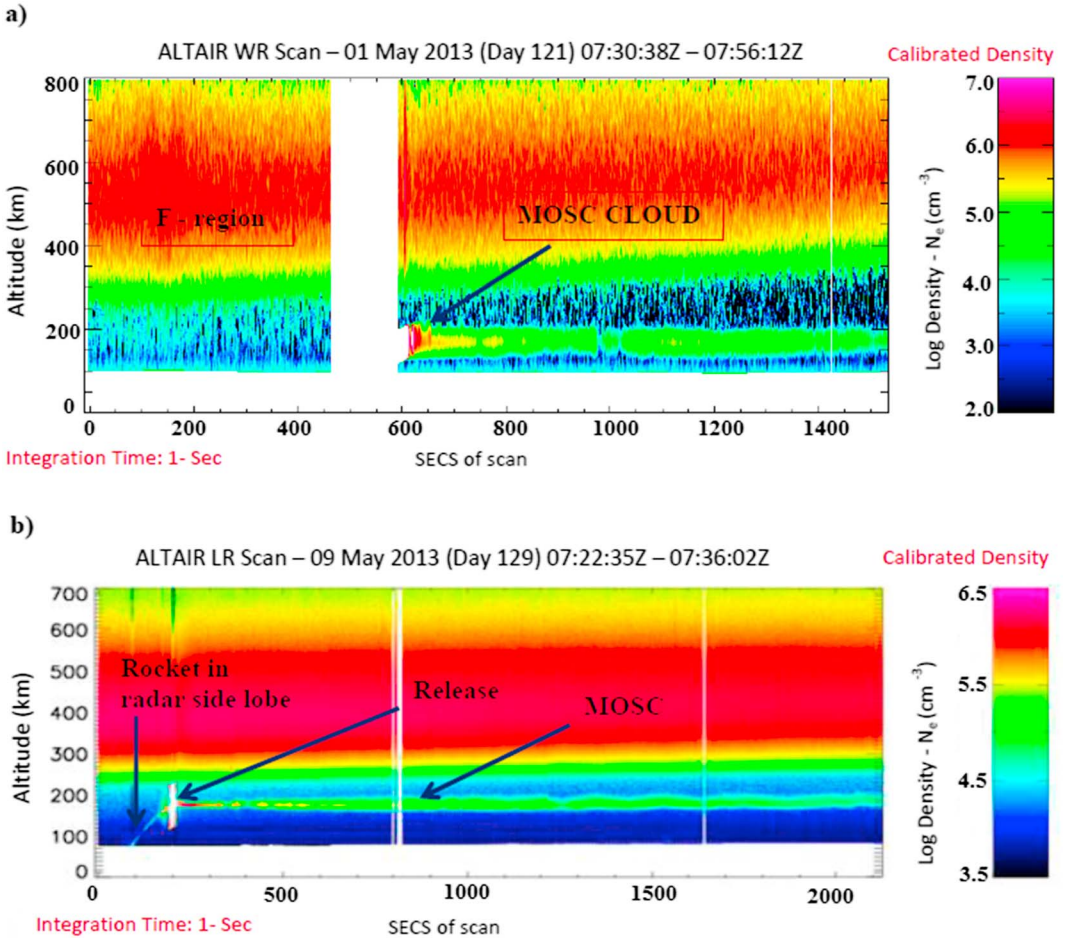

Figure 2. (a) First release: (top) the ALTAIR radar range-time-intensity (RTI) plot shows a rapidly rising *F*-layer of the ionosphere (disturbed condition). (b) Second release: (bottom) the RTI plot shows a quiescent ionosphere typical of the equatorial region just prior to the onset of the prereversal enhancement period.

and *F* region trace is smaller along the Likiep-Wotho path compared to the Rongelap-Wotho path, the reason of which is explained in section 4.2. A more detailed description of the cloud's evolution can be found in *Pedersen et al.* [2017]; here we focus on modeling the HF propagation observed during the first few minutes after the release. The SmO+ plasma also triggered significant modification of HF propagation in the *F* region.

In the first postrelease frequency sweep initiated less than 40 s after the release on 1 May, the Likiep-Wotho path has an MOSC signature only in the high end of the frequency sweep above $f = 8$ MHz (Figure 3d), yet the Rongelap link shows a robust signature beginning at less than 4 MHz (Figure 3c). The subsequent sweep 5 min later shows a solid MOSC trace at lower frequencies only on both paths (Figures 3e and 3f). Moreover, MOSC signature is present across most of the frequency bands on both links in the second release during all phases of the observations (Figures 4c–4f). Potential reasons for the lack of signals on the Likiep-Wotho path in the lower portion of the HF frequency band during the first release will be discussed later in this paper.

3. Modeling

Since *Haselgrove* [1955] set down the differential equations governing raypaths in an anisotropic medium for numerical integration techniques [*Haselgrove*, 1955], the equations have been used extensively [*Jones and Stephenson*, 1975; *Coleman*, 1993; *Zawdie et al.*, 2016] to study the propagation of HF energy through the ionosphere. In our work to model the HF sounder observations, we have used PHaRLAP, a HF radio wave ray tracing MATLAB toolbox developed by Dr. Manuel Cervera, that contains a variety of ray tracing engines of various sophistications from 2-D ray tracing to full 3-D magnetoionic ray tracing [*Cervera and Harris*, 2014].

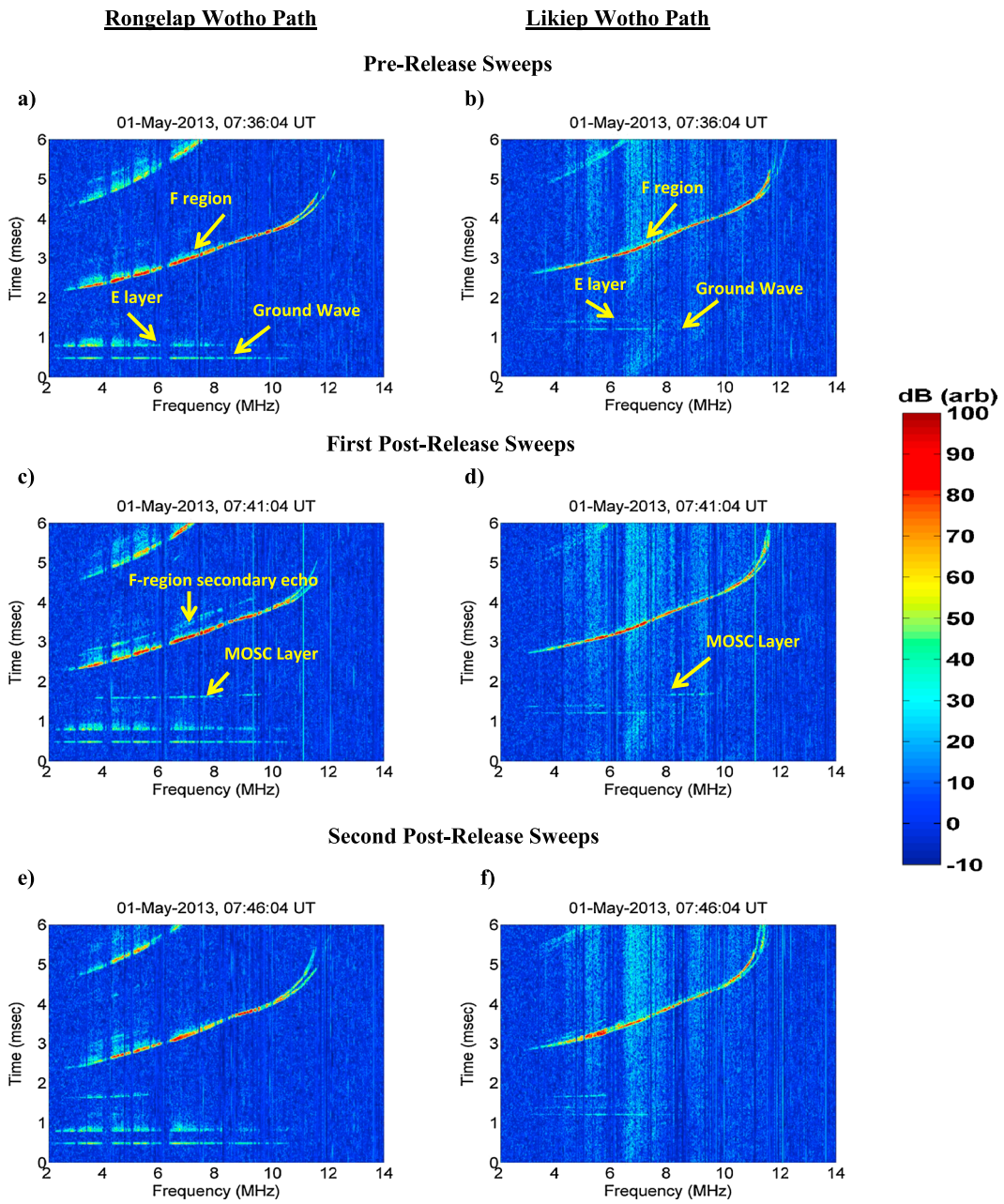

Figure 3. First release: sounder observations of the ionosphere before and after the release of the samarium metal vapor (a, c, and e) along Rongelap-Wotho path and (b, d, and f) along Likiep-Wotho path.

Modeling the sounder observations involved insertion of a three-dimensional plasma cloud representing the MOSC into a background ionosphere and then using full 3-D magnetoionic ray-tracing to understand the various propagation modes induced by introduction of Sm+ ions in the ambient plasma. Prior to the first release on 1 May the ionosphere was rising rapidly ($v_z \geq 50$ m/s), potentially responding to a minor magnetic perturbation ($Dst \sim -50$), and spreads F formed within minutes after the release as observed in the sounder data and ALTAIR radar scan. For the second release, the ionosphere was quiescent as seen in the sounder observations and the radar scan. Hence, we present the modeling efforts for the background ionosphere and samarium cloud for the second release in section 3.1 before those for the first release (section 3.2).

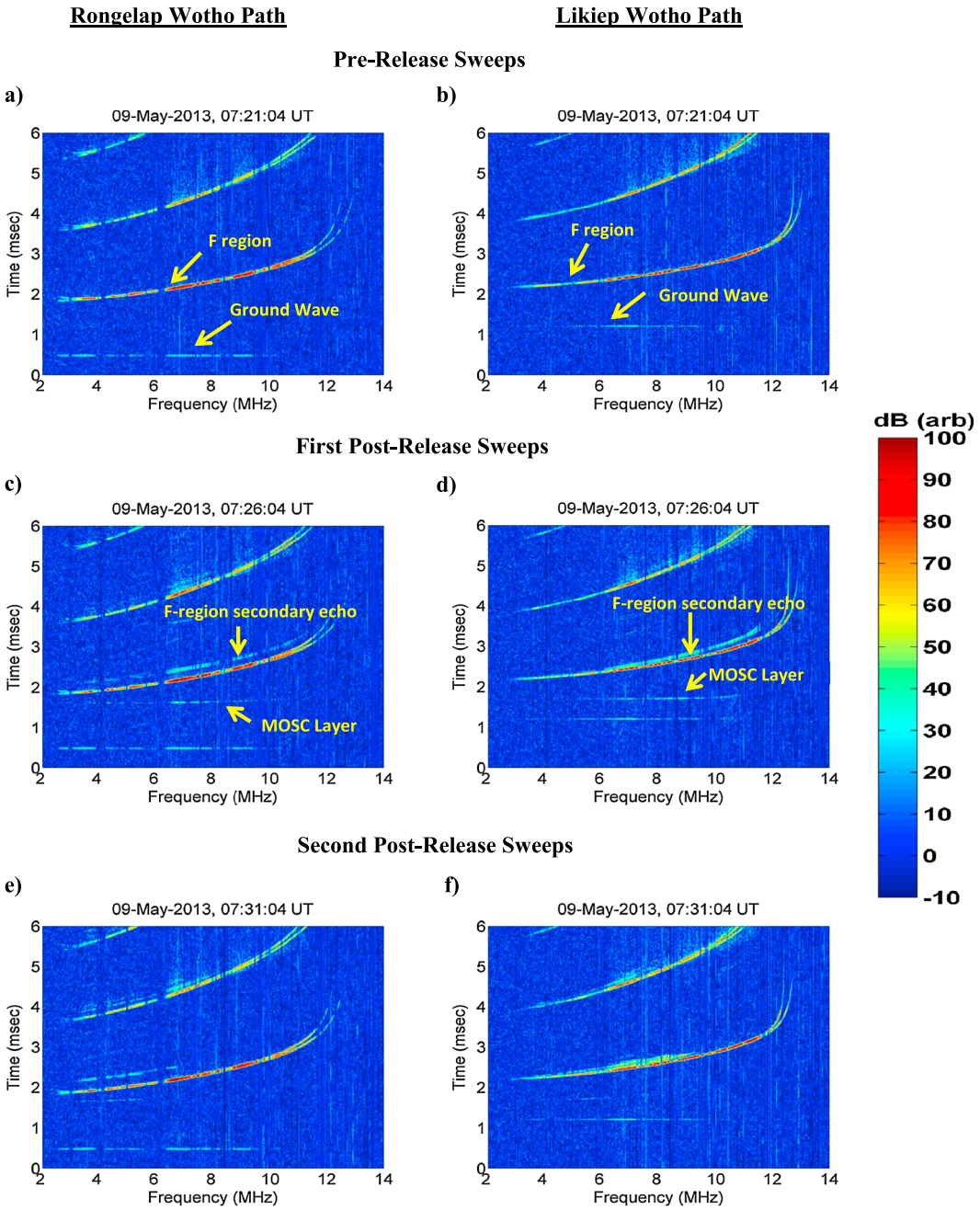

Figure 4. Second release: sounder observations of the ionosphere before and after the release of the samarium metal vapor (a, c, and e) along Rongelap-Wotho path and (b, d, and f) along Likiep-Wotho path.

At early times immediately after the release, the cloud appeared to be symmetric optically and the ALTAIR radar scan also showed a symmetric density profile [*Caton et al.*, 2017]. Before- and after-release density profiles along with the symmetric 3-D representation for the samarium plasma cloud derived from ALTAIR are shown in Figure 5 where a prerelease electron density profile (Figure 5a) and a postrelease profile (Figure 5b) clearly show the contribution of the samarium plasma. A model cloud based on these observations was inserted into the background ionosphere for ray-tracing. A graphical representation of the digitized cloud is shown in Figure 5c, while a false-color image of the cloud itself is shown in Figure 5d. The image was acquired with the AFRL bare CCD camera through a 630 nm filter approximately 4 min after release. The cloud still appears spherical at this time which corresponds to the end of the first postrelease HF frequency scans presented in Figure 4.

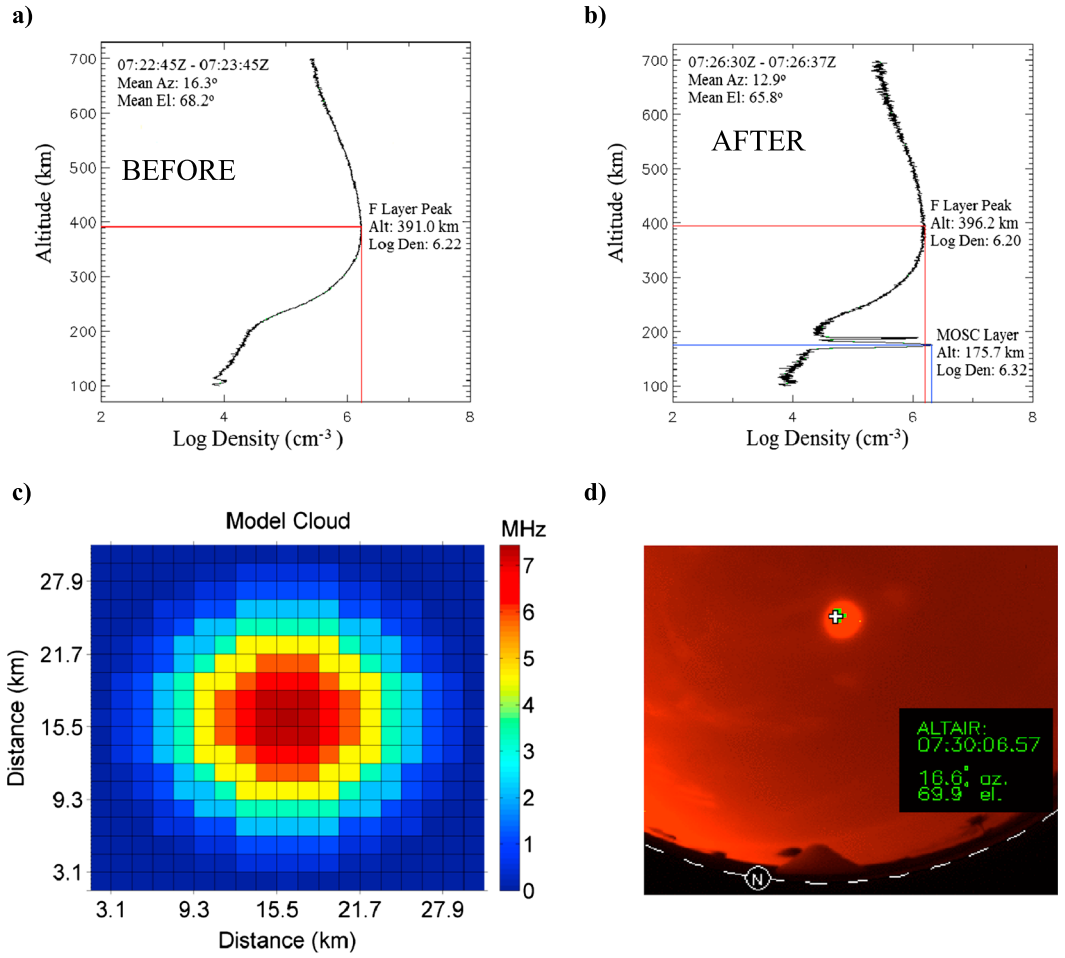

Figure 5. (a) The ALTAIR radar profile before the release of the samarium metal vapor. (b) The radar profile approximately 30 s postrelease. (c) The two-dimensional view of the model cloud through its center is shown. The central pixel corresponds to f_{pe} = 7.44 MHz. (d) A false-color image of the illuminated cloud acquired with the AFRL bare CCD all-sky imager approximately 4 min after release on 9 May 2013. The cross-hair indicates the look-angle of the ALTAIR radar.

An ionospheric model was used for the background because we did not have adequate knowledge of the ionosphere across the whole region of interest. The approach was to constrain the background model with calibrated ALTAIR radar observations at a specific location and then use the model to represent the ionosphere across a region that extended approximately 200 km north and ±200 km E-W from the point of the radar observations. We used the Parameterized Ionospheric Model (PIM) [*Daniell et al.*, 1995] and the International Reference Ionosphere (IRI-2012) [*Bilitza et al.*, 2014] as the background model ionospheres for ray-tracing. The reason for using two models rather than just one will be made clear shortly.

The IRI is an empirical model ionosphere developed as a joint project of the Committee on Space Research and the Union Radio Scientifique Internationale. For a given location, time, and date, IRI provides the median monthly values of electron density, the electron temperature, and ion composition in the altitude range from 50 km to 2000 km. The major data sources for the IRI model are the worldwide network of ionosondes, the powerful incoherent scatter radars, (Jicamarca, Arecibo, Millstone Hill, Malvern, St. Santin), the International Satellites for Ionospheric Studies and Alouette topside sounders, and in situ instruments on several satellites and rockets.

The PIM is a global ionospheric and plasmaspheric model based on combined output from the Global Theoretical Ionospheric Model for low and middle latitudes. PIM produces electron density profiles between 90 and 25,000 km altitude, in addition to other profile parameters such as corresponding critical frequencies and heights for the ionospheric E and F_2 regions, and total electron content.

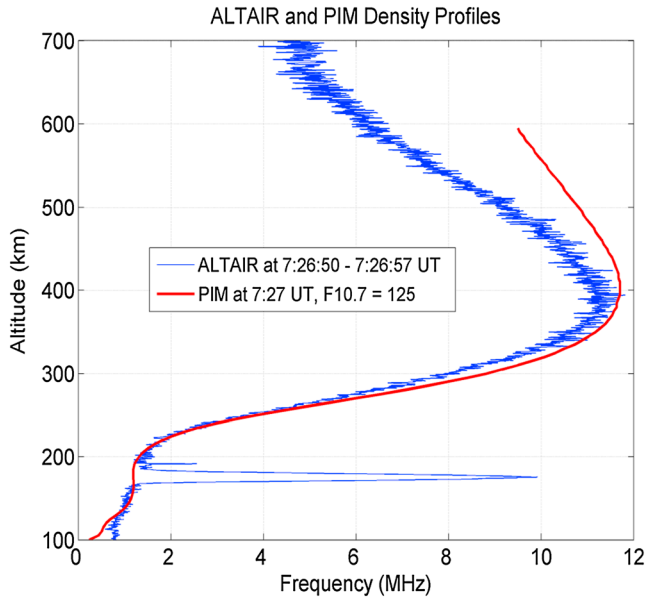

Figure 6. PIM and ALTAIR radar electron density (N_e) profiles displayed as equivalent plasma frequency ($f_p \approx \sqrt{N_e}$, in MKS units). The PIM bottomside fits well with the observed ATLAIR profile. The disparity below about 125 km corresponds to a very low density/frequency ($<10^3$ cm^{-3}/1 MHz) that will not have an appreciable effect on radio waves propagating above about 2 MHz.

3.1. Ionospheric Model for Samarium Release on 9 May

For the second release in which the background ionosphere exhibited typical quiescent characteristics, good agreement between the PIM model and the ALTAIR radar observations were obtained by making a small change in the F10.7 flux input to the model, as shown in Figure 6. The objective was to obtain a good fit primarily to the bottomside to ensure accurate HF propagation modeling.

3.2. Ionospheric Model for Samarium Release on 1 May

For the first release which had a disturbed and rapidly rising ionosphere, no standard model could be fitted to match the background ionosphere. We tried to minimize the difference between the model ionospheric profile and the ALTAIR radar profile at the MOSC release location by an optimization technique known as the Nelder-Mead Downhill Simplex method [*Nelder and Mead*, 1965; *Press et al.*, 2007]. We used the native "fminsearch" function in MATLAB to optimize the difference between the ALTAIR radar ionospheric profile and the model profile (Figure 7a). Since PIM did not have enough accessible degrees of freedom, this optimization technique gave good results only with the IRI model. An altitude-dependent scale vector was obtained by dividing the optimized IRI profile by the initial IRI profile, and this was subsequently used to scale the entire IRI 3-D grid. However, when the optimized results were used on the Rongelap-Wotho path (~150 km NW of ALTAIR scan), the modeled delay did not match observations with sufficient accuracy, presumably because the disturbed ionosphere gradients were not well represented by the scaled climatological model output. After experimenting with a number of approaches we succeeded in modeling the background ionosphere along the ray-path by applying frequency-specific multipliers to the altitude-dependent scale vector; results are shown in Figure 7b. The variations in the multipliers were not large, but they facilitated a good fit between the modeled and observed profiles. The multipliers were determined by adjusting the ionosphere using ray tracing to minimize the difference between the observed and modeled signal delays. The primary objective is not to develop a good model of the ionosphere, but rather, to optimize our ability to model the HF propagation environment. The priority is for the primary *F* region modes to match the observations with high fidelity, so when the samarium cloud is introduced one can have high confidence in the propagation model results.

4. HF Propagation Modeling Results and Discussion

Ray-tracing was performed for both the releases after inserting the 3-D plasma cloud into the background ionosphere. It confirmed and explained the changes in propagation modes of the HF radio waves due to the artificial plasma cloud.

4.1. Rongelap-Wotho Path

As shown in Figure 8a, the Rongelap-Wotho path is nearly N-S and the release point is well off the great circle path connecting the two atolls. Up to three additional paths due to the presence of the samarium plasma cloud for the received HF energy have been identified. Rays reflected directly from the transmitter off the cloud account for the low delay MOSC trace. Meanwhile, the secondary *F* region traces may be formed in two ways. One path consists of reflection first by the *F*-layer to the MOSC cloud and subsequent reflection

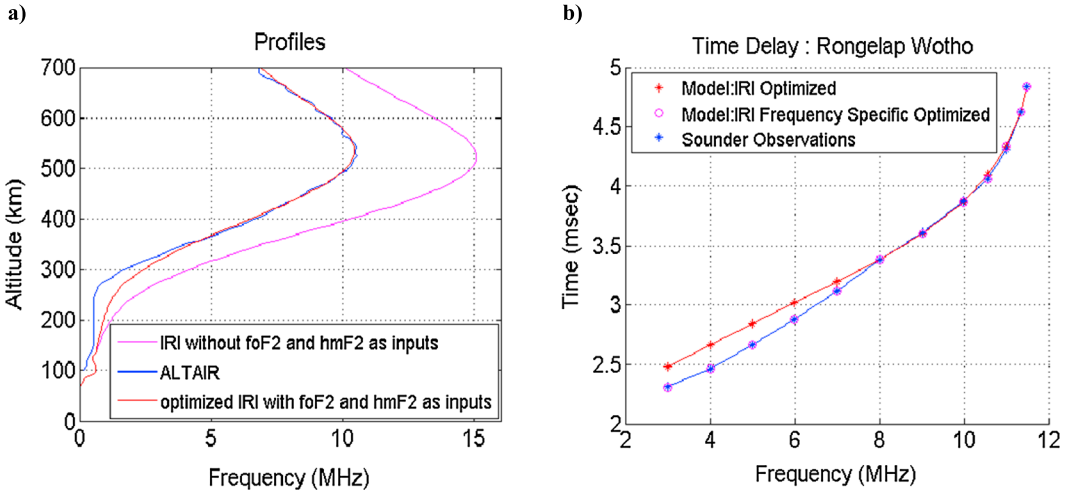

Figure 7. (a) The Nelder-Mead Downhill Simplex method applied to optimize IRI in the vicinity of ALTAIR radar data. (b) A second frequency-dependent optimization procedure was applied to assimilate the sounder data along the R-W path.

to the receiver site (high elevation). The other path is defined by waves that propagate directly to the samarium cloud, reflect to the *F* region, and are then reflected to the receiver (low elevation). The elevation angles so defined refer to the angle between the transmitted HF signal and the ground at the transmitter. Figure 8b shows a graphical representation of the various propagation modes identified to model the time delays shown in Figure 8c. The match between the observations and the model results suggests that both the high- and low-elevation angle paths contributed to the observed *F* region secondary layers. We note that the low-elevation propagation mode corresponds to smaller delay compared to that of the high-elevation propagation mode in the *F* region secondary trace (Figure 8c). This is as expected as the low-elevation mode has a shorter path. From the geometry all the observed signatures confirm that the cloud scattered and/or refracted HF energy well off the great circle path. Rays were traced for a number of selected frequencies. Ray-tracing gave excellent results which agree with the sounder observations (Figures 8c and 8d). For the first release (Figure 8d), the additional MOSC and *F* region secondary layers are also modeled to be close to the observed layers validating the modeling approach and the technique developed to build a disturbed background ionosphere.

For both releases, the sounder observations show greater frequency extent for both the MOSC samarium layer and the *F* region secondary layer than the model results. Reasons for the discrepancy include inadequate spatial resolution of the MOSC plasma cloud in the model and a low estimate of the peak plasma density in the cloud obtained from the radar observations. The high-density center of the cloud is contained in a layer just a few hundred meters on a side, which represents a very small target for ray tracing calculations, particularly for accurately homing rays from a transmitter to a receiver. In fact, it is challenging to resolve the structure adequately in both space and time with the ALTAIR radar. The observations presented in Figure 5b are the true cloud density convolved spatially with the radar beam width and pulse resolution and the time period over which the measurements were integrated. The measurements provide a good estimate of the average parameters of the cloud over a 60 s window, but they do not represent a precise characterization of the plasma cloud at the subkilometer resolution needed to describe the structure in full detail. This does not present a critical problem, however, because the primary objectives to identify and characterize the new propagation modes introduced by the cloud can be achieved without an extremely high fidelity representation of the electron density in the cloud. The radar-derived spatial and plasma parameters are sufficient for this purpose.

4.2. Likiep-Wotho Path

Similar analysis was performed along the Likiep-Wotho path, shown in Figure 9a. This path was selected because the samarium release point lies nearly at the midpoint of the great circle path between the transmitter (Likiep) and the receiver (Wotho). The same modes to/from the cloud and the *F* region were observed in

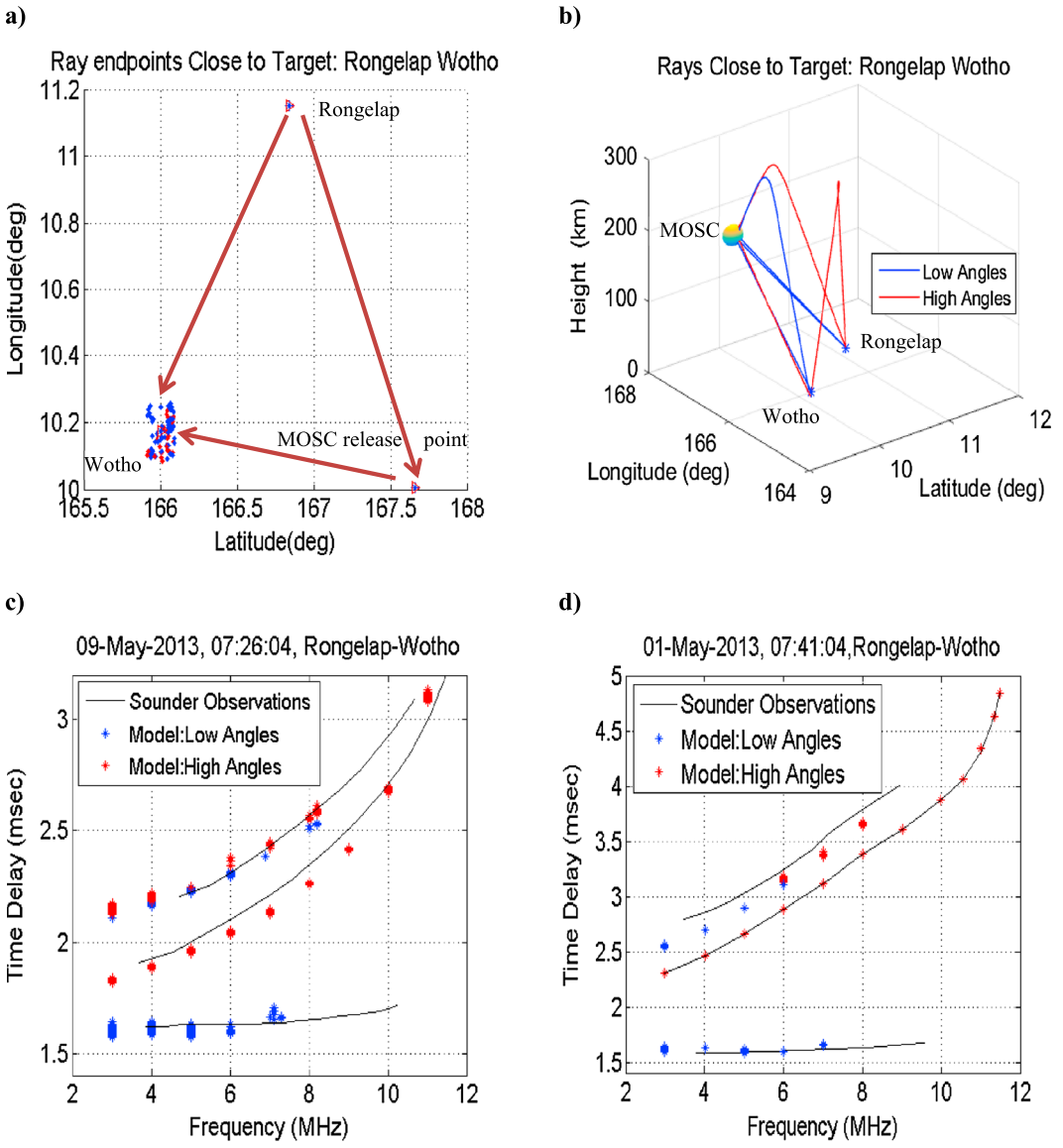

Figure 8. (a) Rongelap-Wotho geometry. (b) Various propagation modes for 6 MHz in second release. Excellent agreement between model and observations: (c) second release and (d) first release.

this geometry, but the differences in delay between the normal *F*-layer path and the delayed paths (*F* region to cloud; cloud to *F* region) were significantly smaller than for the Rongelap-Wotho geometry as expected due to the coplanar geometry (see Figure 9b). Rays traced for various frequencies reproduced the additional MOSC and *F* region secondary layers close to the observations for both releases (Figure 9). As mentioned previously, one significant feature of the observations that remains to be explained is the absence of lower frequency signals (below ~8 MHz) refracted directly from the samarium cloud to the receiver on the Likiep-Wotho path within the first few minutes postrelease on 1 May 2013.

The lack of lower frequency signals on the nearly great circle path is noteworthy because relatively strong lower frequency signals are observed on the distinctly nongreat circle Rongelap-Wotho link at the same time. Moreover, lower frequency signals are present on both links throughout the observing period during the second release on 9 May. One possible explanation is enhanced absorption during the early scan period on the Likiep-Wotho path. This absorption is frequency-dependent and would normally be associated with an enhanced *E*- or *D* region not expected to be present at the time of the observations (18:47 SLT). A

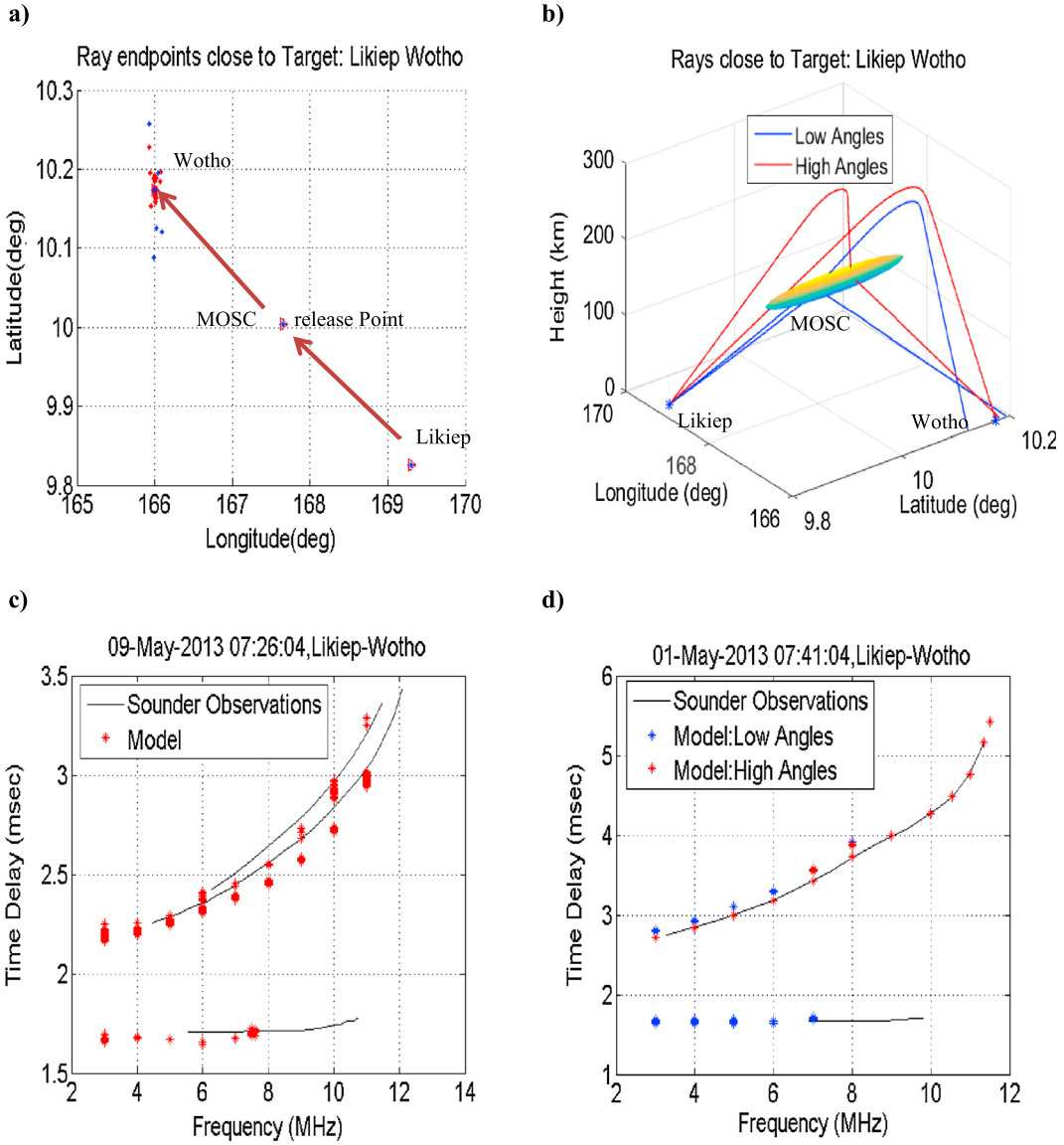

Figure 9. (a) Likiep-Wotho geometry. (b) Various propagation modes for 6 MHz in second release. Close agreement between model and observations: (c) second release and (d) first release.

comparison of the relative intensities of the *F* region traces at frequencies below 8 MHz clearly shows that there is little to no difference between the first and second postrelease scans on 1 May or the scans from the second release on 9 May. Absorption does not appear to be a viable mechanism for the observed absence of power.

The primary geophysical difference between the 1 May and the 9 May releases was the presence of sporadic *E* (Es) on the night of the first release. A reasonably strong Es layer is visible on the Rongelap-Wotho link (Figures 3a, 3c, and 3e) extending to about 10 MHz frequency. A faint Es trace may be observed during the same time on the Likiep-Wotho path. On neither path does the layer appear to be blanketing in terms of masking the *F* region returns or the return from the samarium cloud on the Rongelap path. But that does not preclude the possibility that the path to the samarium cloud from Likiep, which is significantly different than the direct paths to both the *F* and *E* regions, may have been partially or wholly obscured by local sporadic *E* at the lower frequencies consistent with the lack of power observed below 6 MHz on the night of 1 May.

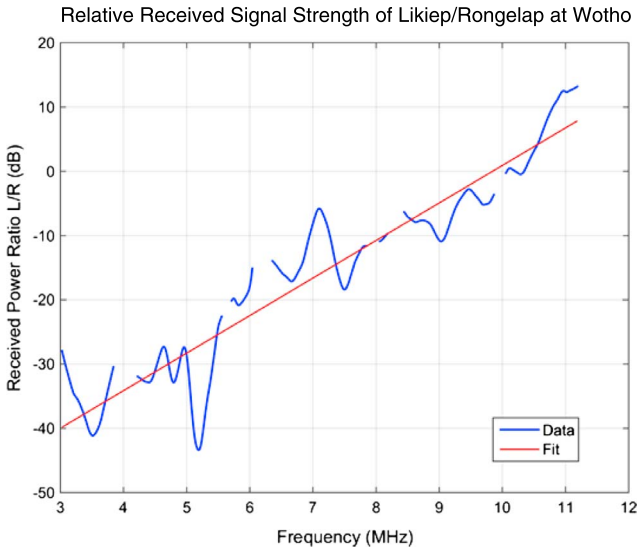

Figure 10. HF power received at Wotho from Likiep relative to Rongelap as a function of signal frequency (Likiep/Rongelap). The straight line shows a linear fit of the data. The received power from Rongelap was considerably higher at low frequencies.

The severity of the effect may have been exacerbated by the reduced received power at low frequencies on the Likiep-Wotho path relative to the Rongelap-Wotho path. HF transmissions at Likiep were weaker overall than those from Rongelap and considerably weaker at frequencies below 8 MHz. In fact, between 2 and 6 MHz the observed average signal strengths at Wotho were more than 20 dB below the corresponding signals from Rongelap, as shown in Figure 10. The curve in the figure shows the ratio of power from Likiep/Rongelap as a function of frequency and was derived from averaging 10 scans during different quiet periods characterized by an absence of spread *F* and low *E* region density. A straight line fit to the data is also plotted to demonstrate the trend of the frequency dependence. Differences in path length between the two sites account for some of the observed SNR differences, approximately 6 and 2.5 dB for *E* and *F* region paths, respectively. A more significant contribution to the disparity may result from the transmit antenna installations at the two sites. The antenna at Rongelap was mounted on a tower some 18 m above ground, while the Likiep antenna was suspended from trees at a height of just 4 m. Although we do not have sufficient details to calculate the exact differences in gain at the two sites, it is well known that the impedance of a dipole antenna changes dramatically as the installation height decreases below one-fourth wavelength (see, e.g., *ARRL Antenna Handbook* [*American Radio Relay League*, 1974]); the resulting impedance mismatch greatly reduces the radiation efficiency of the antenna. The 18 m height of the antenna at Rongelap corresponds to one-fourth wavelength at about 4.2 MHz; the 4 m high antenna at Likiep would transmit much less efficiently at this frequency, though the relative response would be expected to improve rapidly as the frequency increases, as has been observed. Similarly, one would expect the masking efficiency of Es to decrease as the transmitted frequency increases. Thus, we believe that a combination of factors including path length, antenna efficiency, and Es masking effectiveness was responsible for the absence of lower frequency signals scattered by the samarium cloud from Likiep on the evening of 1 May. Of course, differences in the path lengths and antenna efficiencies were common to all the observations, while sporadic *E* was present only during the first release. However, the reduced signal strengths imposed by the common propagation factors from Likiep mean that relatively modest Es masking is needed to explain the observations.

A high-density plasmasphere placed in a low-density plasma background behaves as a divergent lens for radio waves; the signals will always be refracted away from the center. Figure 11 (top) shows such a simulated sphere, while Figure 11 (bottom) displays the relative signal strength for an 8 MHz plane wave traveling from left to right in the figure. The propagation results, derived from a wave-optics calculation [*Hocke and Igarashi*, 2003], show clearly how the power diverges as the wave propagates through the sphere. In this scenario it is plausible that the power from waves below 8 MHz was refracted off axis passing through the samarium cloud and was not received along the great circle path at Wotho; signals at higher frequencies would suffer less refraction and could thus reach Wotho. Meanwhile, the same plasma cloud could refract (or scatter) energy through acute angles such that signals from Rongelap were observed far off the great circle path, consistent with the actual observations. A detailed analysis of the cloud and geometry for the MOSC releases was performed. The results show that the region where refractive effects would be most effective in creating a signal void ("shadow") lies beyond Wotho. Indeed, the ray tracing results shown in Figure 9d specifically predict a signature at the lower frequencies where none is observed. Although it is treated as a sphere in our

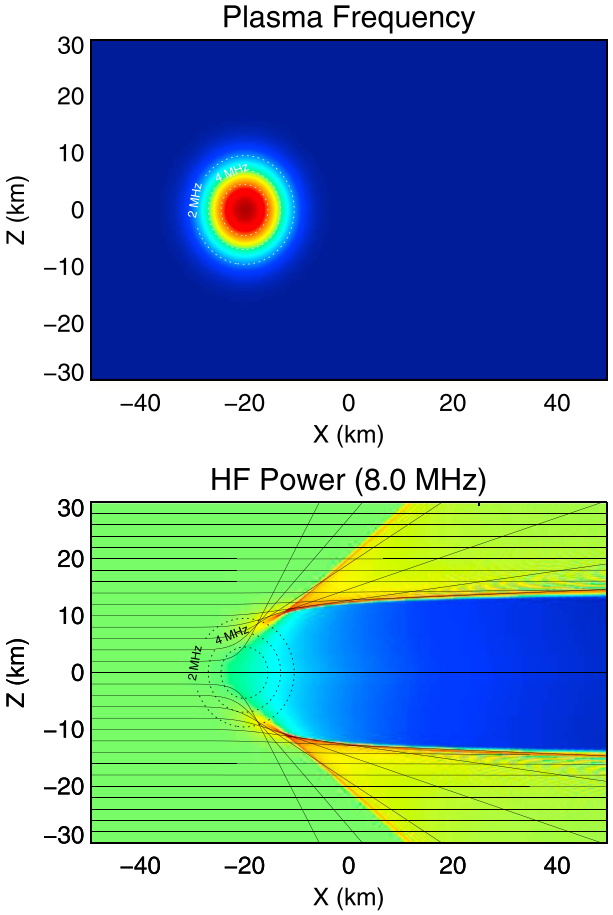

Figure 11. (top) Background environment and plasma distribution for a spherical artificial cloud. (bottom) Wave-optical calculation for 8 MHz radio wave propagation through the artificial cloud.

model, the actual shape and density distribution of the cloud determine the detailed HF propagation effects. Some elongation along the magnetic field is expected, even at early times, and the true shape undoubtedly differs from our simple model. Interestingly, the divergent effects of the cloud would be expected to persist much longer than the effects visible on the oblique ionograms shown in Figures 3 and 4. The divergence effect requires only small refraction angles along the direction of propagation, while large refraction angles are required to generate traces directly from the artificial plasma cloud. Thus, even signals at frequencies well above the maximum plasma frequency in the cloud will experience some level of divergence as they pass through.

5. Conclusions

The results presented here account for the features of the modified HF propagation environment observed at early times during the MOSC samarium release experiments. We have shown that ray tracing techniques may be used to model the disturbances caused by artificial ionospheric modification. The samarium plasma clouds created at least three additional HF propagation paths in the ionosphere. One path is directly from the transmitter to the cloud to the receiver, while two others involve propagation between the *F* region and the cloud: in one case interacting with the cloud first, reflecting off the *F* region to the receiver, and in the other reflecting from the *F* region first and then reaching the receiver antenna by refraction from the cloud. These effects were observed both on a great circle path and a markedly nongreat circle path where the refraction angle exceeds 90°. Additionally, a dropout in the lower portion of the HF band was observed on the great circle path between Likiep and Wotho minutes after the first release. An analysis of several potential causes reveals that the most probable explanation is masking due to sporadic *E* which is exacerbated by the greater distance from Likiep to Wotho and the lower transmitted signal power relative to Rongelap.

For modeling the background plasma, when constrained by ALTAIR radar electron density profiles, the Parameterized Ionospheric Model (PIM) provided an excellent representation of the low-latitude ionosphere during quiet conditions. Not surprisingly, neither PIM nor IRI was able to accurately specify local gradients during a modest magnetic disturbance. However, IRI's flexibility and convenient access to parameters within the model supported the use of a minimization technique for constructing a valid regional ionosphere. Ray-tracing confirms the sounder observations to a high degree of fidelity. Changes in the natural propagation environment can thus be successfully modeled, and the effects from arbitrary artificial plasma environments can be predicted with accuracy. Finally, though not observed directly in these measurements, modeling predicts that the samarium cloud will behave like a divergent lens resulting in "HF voids" or shadow zones where the HF signal is excluded downstream from the sphere. For the geometry in the present experiment the shadow zones are predicted to lie beyond the range of the most distant receiver site, but such effects could readily be characterized in future experiments.

Acknowledgments
The authors from the Boston College Institute for Scientific Research gratefully acknowledge support through the Naval Postgraduate School from the National Consortium for Measurement and Signature Intelligence (MASINT) Research Program award N00244-12-1-0049. We would also like to acknowledge the valuable contributions of the reviewers to this manuscript, specifically in regard to the role of sporadic *E* in interpreting the propagation results (reviewer #2). We would like to thank the U.S. Department of Defense Space Test Program for their support in providing the launch vehicles and launch support for the MOSC payloads. Requests for access to data collected during the MOSC experiment will be processed on a case-by-case basis pursuant to official Air Force Research Laboratory policy for public release of information.

References

American Radio Relay League (1974), *The ARRL Antenna Handbook*, 13th ed., edited by G. Hall, pp. 49–57, American Radio Relay League, Newington, Conn.

Bedinger, J. F., E. R. Manring, and S. N. Ghosh (1958), Study of sodium vapor ejected into the upper atmosphere, *J. Geophys. Res.*, *63*(1), 19–29, doi:10.1029/JZ063i001p0019.

Bernhardt, P. A. (1987), A critical comparison of ionospheric depletion chemicals, *J. Geophys. Res.*, *92*(A5), 4617–4628, doi:10.1029/JA092iA05p04617.

Bernhardt, P. A., et al. (2012), Ground and space-based measurement of rocket engine burns in the ionosphere, *IEEE Trans. Plasma Sci.*, *40*, 1267–1286, doi:10.1109/TPS.2012.2185814.

Bilitza, D., D. Altadill, Y. Zhang, C. Mertens, V. Truhlik, P. Richards, L.-A. McKinnell, and B. Reinisch (2014), The International Reference Ionosphere 2012—A model of international collaboration, *J. Space Weather Space Clim.*, *4*, A07, doi:10.1051/swsc/2014004.

Caton, R. G., et al. (2017), Artificial ionospheric modification—The Metal Oxide Space Cloud experiment, *Radio Sci.*, *52*, doi:10.1002/2016RS005988.

Cervera, M. A., and T. J. Harris (2014), Modeling ionospheric disturbance features in quasi-vertically incident ionograms using 3-D magnetoionic ray tracing and atmospheric gravity waves, *J. Geophys. Res. Space Physics*, *119*, 431–440, doi:10.1002/2013JA019247.

Coleman, C. J. (1993), A general purpose ionospheric ray tracing procedure, Tech. Rep., SRL-0131-TR, Defence Science Technology Organization, Adelaide, Australia.

Corliss, W. R. (1971), NASA sounding rockets, 1958–1968: A historical summary, Tech. Rep. NASA SP- 4401, National Aeronautics and Space Administration, Washington, D. C.

Davies, K. (1990), *Ionospheric Radio*, pp. 143–146, Peter Peregrinus, London, U. K.

Davis, T. N. (1979), Chemical releases in the ionosphere, *Rep. Prog. Phys.*, *42*, 1565, doi:10.1088/0034-4885/42/9/003.

Daniell, R. E., Jr., L. D. Brown, D. N. Anderson, M. W. Fox, P. H. Doherty, D. T. Decker, J. J. Sojka, and R. W. Schunk (1995), Parameterized ionospheric model: A global ionospheric parameterization based on first principles models, *Radio Sci.*, *30*(5), 1499–1510, doi:10.1029/95RS01826.

Haselgrove, J. (1955), Ray theory and a new method for raytracing, in *Physics of the Ionosphere*, pp. 355–364, Physical Society, London.

Hocke, K., and K. Igarashi (2003), Wave-optical simulation of the oblique HF radio field, *Radio Sci.*, *38*(3), 1039, doi:10.1029/2002RS002691.

Hu, Y., Z. Zhao, and Y. Zhang (2011), Ionospheric disturbances produced by chemical releases and the resultant effects on short-wave ionospheric propagation, *J. Geophys. Res.*, *116*, A07307, doi:10.1029/2011JA016438.

Jones, R. M., and J. J. Stephenson (1975), A versatile three-dimensional ray tracing computer program for radio waves in the ionosphere, NASA STI/Recon Tech. Rep., 76, 25,476, U.S. Dep. of Commer., Off. of Telecommun., Washington, D. C.

Nelder, J., and R. Mead (1965), A simplex method for function minimization, *Comput. J.*, *7*, 749–756, doi:10.1093/comjnl/7.4.308.

Pedersen, T. R., R. G. Caton, D. Miller, J. M. Holmes, K. M. Groves, and E. Sutton (2017), Empirical modeling of plasma clouds produced by the Metal Oxide Space Clouds experiment, *Radio Sci.*, *52*, doi:10.1002/2016RS006079.

Press, W. H., S. A. Teukolsky, W. T. Vetterling, and B. P. Flannery (2007), *Numerical Recipes 3rd Edition: The Art of Scientific Computing*, pp. 487–555, Cambridge Univ. Press, New York.

Rosenberg, N. W. (1963), Chemical releases in the upper atmosphere (Project Firefly), a summary report, *J. Geophys. Res.*, *68*(10), 3057–3063, doi:10.1029/JZ068i010p03057.

Shuman, N. S., D. E. Hunton, and A. A. Viggiano (2015), Ambient and modified atmospheric ion chemistry: From top to bottom, *Chem. Rev.*, *115*(10), 4542–4570, doi:10.1021/cr5003479.

Wand, R. H., and M. Mendillo (1984), Incoherent scatter observations of an artificially modified ionosphere, *J. Geophys. Res.*, *89*(A1), 203–215, doi:10.1029/JA089iA01p00203.

Zawdie, K. A., D. P. Drob, J. D. Huba, and C. Coker (2016), Effect of time-dependent 3-D electron density gradients on high angle of incidence HF radio wave propagation, *Radio Sci.*, *51*, 1131–1141, doi:10.1002/2015RS005843.